

<sup>1</sup> Highlights

<sup>2</sup> **Antarctic bed topography estimation using a Stochastic Meshless Uncertainty Gridding (SMUG)  
<sup>3</sup> method**

<sup>4</sup> Lenneke M. Jong, Jason L. Roberts, Felicity S. McCormack, Ana C. Fabela Hinojosa

# 5 Antarctic bed topography estimation using a Stochastic Meshless 6 Uncertainty Gridding (SMUG) method

7 Lenneke M. Jong<sup>a</sup>, Jason L. Roberts<sup>a</sup>, Felicity S. McCormack<sup>b</sup> and Ana C. Fabela Hinojosa<sup>b</sup>

8 <sup>a</sup>Australian Antarctic Division, Department of Climate Change, Energy, the Environment and Water, Australia

9 <sup>b</sup>Securing Antarctica's Environmental Future, School of Earth, Atmosphere and Environment, Monash University, Clayton, Kulin Nations,  
10 Victoria, Australia

11

---

## 12 ARTICLE INFO

15 **Keywords:**  
16 Interpolation  
17 spatial data  
18 Antarctica  
19 bed topography

## ABSTRACT

An ongoing challenge in spatial sciences is the generation of gridded datasets for sparsely sampled data with robust estimates of uncertainty. This is particularly the case for datasets of the bed topography beneath the Antarctic Ice Sheet — an area of approximately 12.1 million km<sup>2</sup> — which suffers from sampling biases due to the difficulty of directly observing this vast and remote region. Here, we present a new method for interpolating sparsely and unevenly sampled data: the Stochastic Meshless Uncertainty Gridding (SMUG) method. SMUG uses a point-by-point meshing scheme and Taylor series approximations to generate a large ensemble of estimates of the data field and its corresponding uncertainty at the interpolation point. We apply the SMUG method to estimate the bed topography of the Aurora Subglacial Basin, East Antarctica, finding high skill in the SMUG estimates compared with existing gridded bed products. The robustness of the method is assessed by progressively excluding an increasing volume of observational data. The results demonstrate that the SMUG method offers significant benefit for applications involving sparse datasets where robust uncertainty quantification is critical for informed decision-making and risk assessment.

29

---

## 30 CRediT authorship contribution statement

31 **Lenneke M. Jong:** Conceptualisation, Investigation, Writing - Original Draft . **Jason L. Roberts:** Conceptuali-  
32 sation, Software, Methodology, Investigation, Writing - Original Draft. **Felicity S. McCormack:** Conceptualisation,  
33 Investigation, Writing - Original Draft. **Ana C. Fabela Hinojosa:** Investigation, Writing - Original Draft.

## 34 1. Introduction

35 A key challenge in spatial sciences is constructing datasets that accurately represent continuous fields from discrete  
36 and often sparse observations and interpolation. The choice of an interpolation method that is able to capture the  
37 underlying variability of the field is not necessarily straightforward. This is a particular challenge when considering  
38 the bed topography of the Antarctic Ice Sheet, where the logistical challenge of obtaining observations means it remains  
39 sparsely sampled. At present, for a 500 m by 500 m horizontal grid, less than 7% of Antarctica's topography across  
40 the 12.10 million km<sup>2</sup> of grounded ice area is sampled by observations (Pritchard et al., 2025), and there are large data  
41 gaps in dynamic regions along the grounding line (Kenichi Matsuoka). This has implications for the propagation of  
42 uncertainties in model projections of Antarctica's evolution under climate change, including the timing and rate of any  
43 potential grounding line retreat (McCormack et al., Submitted).

---

ORCID(s): 0000-0001-6707-570X (L.M. Jong); 0000-0002-3477-4069 (J.L. Roberts); 0000-0002-2324-2120 (F.S. McCormack);  
0009-0000-7238-5761 (A.C. Fabela Hinojosa)

44 Several established interpolation methods have been used to generate Antarctic topography datasets. Here, we focus  
 45 on methods that produce elevation-preserving bed topographies, i.e., where the measurements of the bed topography  
 46 are retained in the gridded dataset produced by the interpolation, rather than methods that preserve other characteristics,  
 47 such as texture or roughness (e.g. Graham et al., 2017; MacKie and Schroeder, 2020; MacKie et al., 2021). One of  
 48 the earliest gridded bed topography datasets for Antarctica — Bedmap1 (Lythe and Vaughan, 2001) — employed an  
 49 Inverse Distance Weighting (IDW) algorithm. This method estimates values at unsampled points as weighted averages  
 50 of nearby measurements, with weights inversely proportional to a power of distance (e.g., weight =  $1/\text{distance}^p$ ,  
 51 where  $p$  is the power parameter, Mitas and Mitasova, 1999). In Bedmap1, the IDW algorithm uses the nearest two  
 52 observations in each octant (a total of up to 16 data points) to estimate the value at each grid node. The octagonal  
 53 approach was specifically designed to address the highly anisotropic distribution of the ice thickness survey data.  
 54 After evaluating different weightings, Lythe and Vaughan (2001) found that inverse-cubed weighting produced the most  
 55 plausible surface for the given data distribution. While IDW is straightforward to implement, computationally efficient,  
 56 and honours all measurements, the impact of the power parameter on results can be unintuitive, particularly when  
 57 dealing with high variability measurements. That is, lower values of the power parameter may give disproportionately  
 58 high weighting to distant points and obscure local trends. In addition, IDW tends to produce overly smooth surfaces  
 59 by biasing estimates towards the mean, and cannot produce interpolated values that exceed the observed data range.

60 A number of alternatives to the IDW method have been proposed. The most ubiquitous is Kriging, a form of  
 61 Gaussian Process Regression, which employs spatial correlations across a dataset to generate predictions (Webster and  
 62 Oliver, 2007). Comparative testing of the Kriging method was evaluated during the development of both Bedmap2 (Fretwell  
 63 et al., 2013) and Bedmap3 (Pritchard et al., 2025), and found to produce less accurate interpolations of Antarctic bed  
 64 topography than the adapted spline method used in these well known topography products. Kriging incorporates sta-  
 65 tistical, rather than heuristic, estimates of uncertainty and assumes that spatial distributions can be represented as  
 66 realisations of random functions. However, its implementation often requires human input, particularly for selecting  
 67 model parameters. This means that key decisions, such as choosing variogram models (mathematical functions that  
 68 describe how the similarity between data points changes with distance) and addressing gaps in the data where critical  
 69 surface features may be missing, can be highly subjective. For example, the interpolation methods used in Bedmap1  
 70 and Bedmap2 rely on the assumption that in mountainous areas, where ice fills the valleys, there is a general corre-  
 71 lation between ice thickness and the distance from rock outcrops (Fretwell et al., 2013). The problem with such an  
 72 assumption is the introduction of systematic biases in ice thickness estimates, particularly in regions with complex  
 73 bed topography. These biases can lead to underestimation of bed elevation in deep valleys and overestimation in areas  
 74 with irregular subglacial features, affecting subsequent ice volume calculations. Kriging is particularly effective for  
 75 modelling phenomena with significant random components (Mitas and Mitasova, 1999) and provides robust uncer-

tainty estimates. However, its performance is highly dependent on expert-driven parameter selection, which must be carefully adapted to the specific characteristics of Antarctic bed topography data.

The key technique used in both Bedmap2 and Bedmap3 is Topo-To-Raster (an ArcGIS algorithm that was known as Topogrid at the time that Bedmap2 was generated), an adapted thin plate spline interpolation method that incorporates iterative finite difference interpolation to prevent spurious sinks (Fretwell et al., 2013; Pritchard et al., 2025). To determine the optimal interpolation method to generate Bedmap2, the performance of multiple interpolation methods was compared for a Scottish Highlands test landscape with sampling patterns mimicking Antarctic surveys. Topogrid outperformed both spline-with-tension (85 m standard deviation) and Kriging methods, yielding a standard deviation of 66 m. Despite this superior performance, spline methods do not necessarily honour all data points, so while they produce smooth surfaces, they may overly deviate from observed data points and miss fine-scale structures in the data. Furthermore, optimisation of the smoothing parameters remains challenging. As Fretwell et al. noted, “disparities between varied input data sources, the inhomogeneous spatial distribution of data, and its highly-variable reliability” necessitated “a rather complicated, multi-stepped process of automatic analyses and manual intervention” (Fretwell et al., 2013). Their assessment revealed that interpolation errors vary systematically with terrain type (alpine, low relief, trough, mixed), suggesting that interpolation methods should ideally be tailored to specific landscape morphologies rather than applying a single method uniformly.

Interpolation beyond data points is problematic regardless of the method used. This is particularly challenging for Antarctica, where data coverage is sparse and irregular. In Bedmap2, 66% of cells had no direct measurements and extrapolation was relied upon, increasing the error with increasing distance from observations at a rate of 2–8 m/km. Conservative error estimates in interpolated regions reach  $\pm 300$  m, with the largest errors ( $\sim 1800$  m) occurring when crossing unsampled troughs in high-relief areas (Fretwell et al., 2013).

Mass conservation has been recently developed to address some of the limitations of other methods by incorporating physics-based constraints into the interpolation process. This approach maintains a consistent balance between the surface mass balance (accumulation and ablation), ice flux divergence, and spatial thickness changes throughout the model domain (Roberts et al., 2011). However, these methods require additional input data beyond bed measurements, including surface velocity fields and assumptions about boundary conditions (e.g. the basal friction coefficient in the friction law), which may not always be available. Notably, the BedMachine Antarctica and Greenland datasets implement mass conservation methods and combine radar-derived estimates of ice thickness, gravity-derived bathymetry, ice velocity, and surface mass balance to create high-resolution gridded bed topography datasets (M. Morlighem, 2017; Morlighem et al., 2020) which have revealed previously unknown basal features with significant implications for the assessment of glacier vulnerability. The BedMachine algorithm solves a steady hyperbolic partial differential equation that relates the ice flux divergence and the apparent mass balance (Morlighem et al., 2011, 2020). Here, the apparent

108 mass balance represents the net local gain or loss of ice mass required to reconcile observed ice thickness and flow.

109 While the above methods have proven useful in many applications, they exhibit several limitations that motivate the  
 110 development of new approaches. In particular, many of the above methods lack robust uncertainty estimates, which  
 111 are crucial for understanding the reliability of interpolated values and planning future measurement campaigns. In  
 112 addition, these methods often fail to realistically capture the spatial correlation of errors, which can potentially lead  
 113 to underestimation of uncertainty in regions far from measurements. This highlights the need for new approaches  
 114 that can: (1) accurately reproduce values at measurement points while providing reasonable extrapolation beyond the  
 115 data extent; (2) operate with intuitive parameters that users can confidently adjust based on their understanding of the  
 116 physical system; and (3) provide robust uncertainty estimates that account for measurement errors and interpolation  
 117 uncertainties. Additionally, modern applications increasingly require methods that can handle large datasets efficiently  
 118 while maintaining accuracy across various spatial scales.

119 In this study, we introduce a new ensemble based interpolation algorithm — Stochastic Meshless Uncertainty  
 120 Gridding (SMUG) — for irregularly sampled data. We use this new algorithm to interpolate the bedrock topography  
 121 for the Aurora Subglacial Basin, East Antarctic, whilst simultaneously generating robust uncertainty estimates, and  
 122 compare our bedrock to other recent interpolations. We evaluate the skill of SMUG in this region by performing  
 123 additional SMUG interpolations that exclude observational data within various distances from the interpolation point,  
 124 comparing each realisation with the original SMUG interpolation that incorporates the full observational dataset.

## 125 2. Methods

126 Conceptually SMUG is a point-by-point meshing scheme, where each mesh point is considered independently, and  
 127 an interpolated value is returned if there are no observations at the mesh point. SMUG uses a pool of neighbouring  
 128 observation points (described in section 2.1) and a Taylor series approximation (described in section 2.2) to estimate  
 129 the value and uncertainty of the data field being interpolated at each mesh point. An ensemble of estimates are cal-  
 130 culated, and the inverse-uncertainty-squared weighted central tendency and spread of the resulting ensemble returned.  
 131 The derivatives required for the Taylor series approximation are calculated using the meshless method of Roberts  
 132 (2024), which ensures machine-precision accuracy for randomly located neighbours (compared with most methods for  
 133 estimating derivatives which require regularly-distributed data for high accuracy).

### 134 2.1. Neighbour selection

135 Neighbour selection is a multi-step process. Firstly, a pool of suitable neighbours representing broad angular  
 136 coverage is determined. Then the actual points used for the Taylor series approximation for each ensemble member is  
 137 selected from within this pool.

138 **2.1.1. Neighbour pool**

139 The selection of neighbouring observation points to include in the pool of suitable points is via an angular-  
 140 separation weighted inverse distance greedy algorithm. First, the input data is divided into equi-angular sectors, rotated  
 141 such that the closest observation to the interpolation point of interest is in the centre of the first sector. By default,  
 142 there are eight sectors for a first-order Taylor series approximation and 16 for a second-order approximation, but the  
 143 user can override these defaults. The pool of suitable neighbours will contain a default of four points per sector (again  
 144 the user can override this default). Second, on a sector-by-sector basis, the closest point is included, and the effective  
 145 distance to each remaining point is scaled by a factor  $d_{\text{eff}}$  to penalise points close (in an angular sense) to the points  
 146 in the sector already selected. Here,

$$d_{\text{eff}} = (1 + \exp(-(2\delta\theta/\Theta)^2)), \quad (1)$$

147 where  $\Theta$  is the angular extent of each sector and  $\delta\theta$  the angular separation between the point under consideration  
 148 and the previous point added to the pool from this sector. The next closest point (based on the penalised distance) is  
 149 selected and the process repeated until the required number of points have been added to the pool from each sector in  
 150 turn.

151 **2.1.2. Ensemble member point selection**

152 Each ensemble member uses its own subset of points of  $N$  points drawn from the pool of suitable points (sec-  
 153 tion 2.1.1). By default  $N=4$  for a first order Taylor series approximation, and 8 for a second order approximation, but  
 154 again these defaults can be overridden. If  $N$  is less than the number of sectors, we uniform-randomly select which sec-  
 155 tors to draw a single point from, always including the sector containing the closest point to our point of interest. Then,  
 156 from each chosen sector, we non-uniformly select which point from the pool to include, weighted by the inverse (true,  
 157 not effective) distance squared to the point. If  $N$  is larger than the number of sectors, we then inverse-distance-squared  
 158 weighted randomly select from the remaining points in the pool.

159 Finally, we again randomly choose, using an inverse-distance-squared weighting, which of the  $N$  points to use to  
 160 perform the Taylor series approximation.

161 **2.2. SMUG**

162 The SMUG algorithm is based around a Taylor series approximation (of order 1 or 2, as determined by the user)  
 163 from a subset of size  $N$  points randomly drawn from the pool of suitable neighbouring points (section 2.1) to estimate  
 164 the value of the observational data field of interest, and its associated uncertainty, at the mesh point ( $P$ ) of interest.

165 The Taylor series approximation is conducted from one of the  $N$  neighbours ( $N_T$ ), chosen randomly with an inverse  
 166 distance (to  $P$ ) squared weighting. To simplify the calculations, the  $N$  neighbouring points are translated and rotated  
 167 such that  $P$  is at the origin, and  $N_T$  is on the positive x-axis. The Taylor series estimate ( $T$ ) is then given by:

$$T = \begin{cases} V_T - V'_T * X_T, & \text{for order 1;} \\ V_T - V'_T * X_T + V''_T * X_T^2 / 2, & \text{for order 2.} \end{cases} \quad (2)$$

168 Here,  $X_T$  is the x-axis intercept of the rotated point  $N_T$ ,  $V_T$  is the observation data field of interest at the point  
 169  $X_T$ , and  $V'_T$  and  $V''_T$  the first and second order partial derivatives, respectively, of the observational data field of  
 170 interest calculated in the x direction at the point  $X_T$ . These derivatives are estimated using a meshless method based  
 171 on differential quadrature, radial basis test functions and hyper-dual numbers (Roberts, 2024). The meshless method  
 172 ingests the locations of the neighbouring observational points and calculates a corresponding vector of weighting  
 173 coefficients to be applied to the observational points to estimate the required derivatives. When implementing the  
 174 projection of the gradient given in Equation 2 we use a multi-step approach so that the distance  $X_T$  is subdivided  
 175 into  $m$  intervals. This multi-stage approach is beneficial when the interpolation distances are large and the gradient  
 176 may vary significantly, and improves both the estimate and uncertainty. The derivative is estimated at the start of the  
 177 interval, projected along the length  $\frac{X_T}{m}$  and the process repeated until the interpolation point is reached, taking into  
 178 account changes in the gradient. This increases the effective order of the Taylor series expansion such that it is higher  
 179 than would be the case for a single step approach.

180 For the Taylor expansion around  $N_T$ , the uncertainty is estimated using Ball-Arithmetic (Johansson, 2020). Specif-  
 181 ically, we apply the following three rules to the Taylor series estimates of Equation 2:

$$\begin{aligned} (A_c, A_r) + (B_c, B_r) &= (A_c + B_c, A_r + B_r), && \text{addition;} \\ (A_c, A_r) - (B_c, B_r) &= (A_c - B_c, A_r + B_r), && \text{subtraction;} \\ (A_c, A_r) \times (B_c, B_r) &= (A_c \times B_c, |A_c|B_r + |B_c|A_r + A_r B_r), && \text{multiplication.} \end{aligned} \quad (3)$$

182 Here, two floating point numbers ( $A$  and  $B$ ) are each represented by a pair of numbers  $(c, r)$ , where  $c$  is the centre (best  
 183 approximation), and  $r$  is the (always non-negative) radius (uncertainty) of the floating point ball approximation of a  
 184 real number.

185 To obtain robust estimates of the observational data field of interest and uncertainty at  $P$ , we generate an ensemble  
 186 of estimates and calculate the uncertainty-weighted central tendency and spread using robust statistical measures (M-

estimator for central tendency (Wilcox, 2010) and FQn for spread (Smirnov and Shevlyakov, 2014)): these are more statistically robust equivalents of the mean and standard deviation respectively. Specifically, we generate an ensemble of 500 (default, but user changeable) members using random (but not uniformly) selected points, and calculate the inverse-uncertainty-squared weighted central tendency (M-estimator) and spread (FQn) calibrated to give the standard deviation for normally-distributed data.

## 2.3. Application to East Antarctic Bed Topography

We test the SMUG algorithm using the Bedmap3 observational datasets (Frémard et al., 2023) of bed elevation in a domain of East Antarctica that extends from the West Ice Shelf to Porpoise Bay to the east (Figure 1). The inland limit of the region includes Lake Vostok and Dome C; hence, our domain encompasses the Aurora Subglacial Basin (ASB) and the Denman-Scott catchment, the key outlet glaciers of which (Totten and Denman Glaciers) are among the most rapidly thinning glaciers in East Antarctica (Smith et al., 2020).

The Bedmap3 dataset is collated from radar surveys of Antarctica beginning in the 1950s. Here, we apply the SMUG algorithm to the observational datasets included in the Bedmap3 compilation, which are freely accessible via the UK Polar Data Centre and the SCAR Bedmap Data Portal (Frémard et al., 2023). All original data are provided on a WSG84 Latitude-Longitude grid (EPSG:4326), which we then convert to an Antarctic Polar Stereographic projection (EPSG:3031), referenced to a Standard Parallel of 71°S. We conduct a basic quality check of the bed elevation data, removing several outlier data lines (where bed elevation measurements at cross-over points are inconsistent with the remaining data), specifically lines 18271–19771 from the STANFORD\_1971\_SPRI-NSF-TUD\_AIR\_BM3.csv and segment 2012331\_ASB\_JKB2h\_R11Ec from UTIG\_2010\_ICECAP\_AIR\_BM3.csv.

We apply the SMUG algorithm described in sections 2.1 and 2.2 above to our domain of interest, to derive a gridded bed elevation reconstruction at 500 m, and defined on the same grid as the BedMachine Antarctica version 2 dataset (Morlighem et al., 2020) for comparison with both BedMachine and Bedmap3 gridded bedrock elevation products (Pritchard et al., 2024) .

## 3. Results

### 3.1. SMUG bed elevation and uncertainty

A bed elevation reconstruction for our domain of interest using a Taylor series expansion of order 1 is shown in Figure 1A. The SMUG interpolation captures the known features of the region consistent with other bed elevation products. Much of the ASB bed is below sea level, including the deep trough of the Vanderford Subglacial Trench that separates Law Dome from the main Antarctic continent, through which the Totten and Vanderford glaciers flow, and the marine basin extends far inland. Features above sea level include Highlands A and B. To lessen the effect of

**Table 1**

Summary of differences from published bed topographies.

	mean difference (m)	median difference (m)	standard deviation (m)	Inter-quartile range(m)
SMUG-bedmap3	0.79	-14.64	163.93	87.68
SMUG-bedmachine	4.48	5.87	178.62	115.35

217 artifacts such noise occurring in areas of rapidly changing terrain, we applied a 1 km median filter over the SMUG  
 218 bedrock elevation and extracted the locations of highest and deepest points, finding them to be broadly consistent with  
 219 other bedrock elevation products. The highest point estimated by SMUG is  $2081 \pm 55$  m, in the Vostok subglacial  
 220 highlands to the south-west of Lake Vostok. Other high elevation regions, such as Highlands A and B and Dome C,  
 221 are also resolved. The lowest estimated bedrock elevation occurs in the trough at the front of the Denman Glacier at  
 222  $-2833 \pm 66$  m. The deep bedrock of the Vanderford Subglacial Trench, near the Moscow University Ice Shelf and  
 223 deep channels inland in the Aurora Subglacial Basin are also well resolved.

224 The uncertainties in the bedrock elevation, shown in Figure 1B, are highest where there is greater spacing between  
 225 observational data, such as the large regions to the north-east of Dome C and south-east of Lake Vostok. Large errors  
 226 are also apparent where there are rapid changes in elevation over short distances, such as along the slopes of the deep  
 227 channels in the Denman-Scott region.

228 Figure 1C–D shows the difference between the SMUG-derived bedrock elevation and that of both Bedmap3  
 229 (Pritchard et al. (2025)) and Bedmachine (Morlighem et al. (2020)), noting that except for the exclusion of the data  
 230 outliers listed above, SMUG uses the same observational dataset as Bedmap3.

231 Overall, SMUG is generally in good agreement with both Bedmap3 and BedMachine, with a small bias and mod-  
 232 erate differences (see Table 1). However, SMUG predicts a generally shallower topography than other gridded bed  
 233 products, and larger local differences, particularly in regions where we have sparse data and rough topography, where  
 234 SMUG uncertainty is higher and there is limited data availability.

235 The Denman-Scott region in particular shows marked differences between SMUG and other bed topography inter-  
 236 polation products. Radar coverage is generally good in parts of the region: several surveys conducted perpendicular to  
 237 the flow direction at the Denman Glacier front have a line spacing of 5 km, increasing to 10 km further inland. Flight  
 238 lines also exist along the direction of flow in the Denman Glacier. SMUG estimates a Denman Glacier trough shallower  
 239 than both Bedmap3 and Bedmachine. The steep slopes in deeper parts of this trough result in missing observational  
 240 data where radar reflections are not returned. In particular, along the transect from Ta–Tb (yellow line in Figure 2A–F)  
 241 — a flight line that loses radar reflections across the deeper parts of the trough — the SMUG interpolation is consid-  
 242 erably more shallow, differing from both Bedmap3 and Bedmachine by approximately 2000 m.

243 To further investigate whether the systematic differences between the SMUG interpolation and the Bedmap3 and

244 BedMachine datasets shown in Figure 2G are reasonable, we compared the SMUG bed with the MEaSURES surface  
 245 speed and computed the longitudinal strain rate from the MEaSURES surface velocity in the Denman region (Figure  
 246 2E–F). We see that the flow speed at the location of the Ta–Tb transect is slightly lower than directly up and  
 247 downstream of the transect, suggesting a slight shoaling from a shallower depth at that point. Further evidence of this  
 248 is seen in the pattern of compression and extension in the longitudinal strain rate at the same location.

249 A grid pattern is visible in the Lake Vostok bathymetry, aligning with the 1000 m below mean sea level contour.  
 250 In this region, there are at least two observational survey datasets, which appear to have a vertical offset between their  
 251 observations of bed elevation. The more uniformly spaced survey reports, in general, slightly shallower bed elevations  
 252 compared to the other survey, which has a higher density sampling in the along track, but larger spacing between survey  
 253 tracks. This results in interpolated topography that is in general slightly shallower than the 1000 m contour except near  
 254 the locations of the more spatially anisotropic survey.

### 255 3.2. Skill and bias

256 To investigate the skill and bias of the SMUG algorithm and the robustness of the uncertainty estimates in regions  
 257 of sparse or non-existent data, we generated a series of 1 km resolution interpolations of our domain, excluding any  
 258 observational data within a series of distances to the interpolation point, namely at distances of 5, 10, 20, 30, 40 and  
 259 50 km. The results of this data exclusion exercise are shown in Figure 3, with spatial maps for individual data exclusion  
 260 distances shown in Figure 4. In each case we compare the resultant interpolation with that using all data.

261 The order of the Taylor series expansion used in SMUG is its main user selectable parameter. To demonstrate the  
 262 effect of increasing the order of the Taylor series, we performed a 2nd order Taylor interpolation for the ASB region,  
 263 shown in Figure 5. Compared to the 1st order Taylor interpolation (Figure 1), the higher order interpolation has more  
 264 impulse noise (sudden, short-duration disturbances; also known as “salt and pepper” noise) and higher uncertainty,  
 265 but consistent large-scale features. There is low bias between the two interpolations (mean difference of 2.2 m and  
 266 a median of 0.0 m) and, in general, small differences (standard deviation of 115.6 m and an inter-quartile range of  
 267 57.4 m). The differences tend to be smaller across the deep basins where the bedrock is below mean sea-level, and  
 268 larger over the higher elevation features, although these also tend to be the areas with greater distances between survey  
 269 lines.

## 270 4. Discussion

271 SMUG is a stochastic algorithm that uses random numbers to select combinations of points from a pool of nearby  
 272 observations to use in constructing the ensemble. Therefore, the interpolated data-field (and associated uncertainties)  
 273 will differ slightly between successive applications to the same dataset, except at any points where observations exist.

274 These differences should be small with an appropriately chosen ensemble size (typically around 500 ensemble members  
 275 is sufficient, but this may need to be increased for datasets with particularity challenging distributions). However, larger  
 276 ensemble sizes require more computational resources, with the compute time scaling approximately linearly with  
 277 ensemble size. The majority of SMUG's run-time (with the exact proportion varying with the number of neighbours  
 278 and their spatial distribution) is used in the calculation of the spatial derivatives. The run-time scales linearly with  
 279 the number of ensemble members. The routines used to calculate the ensemble statistics (M-estimator and FQn) have  
 280 a minor impact on run-time, although the run-time for these computations scales non-linearly with the number of  
 281 ensemble members.

282 The selection of observations included when interpolating a point can have significant impact on the quality and  
 283 fidelity of the resulting interpolation. No single interpolation scheme is likely to perform well for all possible combi-  
 284 nations of underlying field and observational sampling, and can lead to artefacts in the resulting interpolated field. The  
 285 scheme used in SMUG — a pool of nearby points with good angular coverage — combined with the stochastic ensem-  
 286 ble, result in a reasonable and skilful interpolation. However, as SMUG considers each interpolation point in isolation,  
 287 if the in-built point selection routine does not perform well in certain situations (e.g. XX?), the user can easily bypass  
 288 the built-in routine by pre-processing the observational data to select  $N$  points using their preferred method.

289 The SMUG interpolation value is calculated by projecting the estimated local gradient. As such, it will perform  
 290 better in situations where that gradient is smooth, and the distribution of observations allow for it to be accurately  
 291 estimated. Therefore, we expect SMUG to perform best in situations where the underlying data field is smoothly-  
 292 varying and sampled sufficiently densely to capture changes in the gradient of that field. When the underlying data  
 293 field is more uneven and sparsely sampled, SMUG's random sampling of the proximal observations, and relatively  
 294 large ensemble size should help minimise any bias, and produce a robust estimation of the uncertainty.

295 As SMUG considers each interpolation point in isolation, impulse noise can occur, although this should be minimal  
 296 with an appropriate ensemble size. This effect is present in our Antarctic bedrock topography example, and is seen to  
 297 be present in the inland region near south-west of Lake Vostok and at the coastal margin between 80 – 85° E. If such  
 298 noise is present, it can easily be removed using a median filter (or similar), although care should be taken to honour  
 299 observational data points when filtering. The resultant topography after applying the median filter is shown in Figure 6.

300 As the exclusion distance increases (i.e. when less data is used in the SMUG interpolation), the ability to accurately  
 301 resolve features decreases (and uncertainty increases). This is seen in Figure 4, where features such as the inland  
 302 Highlands are no longer able to be resolved beyond an exclusion radius of 20 km, and the deep subglacial troughs past  
 303 a 10 km exclusion radius. When comparing the interpolation with the full observational dataset to the cases where  
 304 data is excluded, SMUG shows very low biases and low differences (with a median difference of less than 150 m when  
 305 data is excluded within 50 km). As SMUG uses a Taylor expansion, and therefore projects observed gradients, it is not

surprising that it cannot resolve small-scale (compared to the data exclusion radius) features in the absence of input data. Additional data-streams, such as surface elevation and velocities as used by mass conservation based interpolation schemes (such as BedMachine), are required to resolve features in the absence of proximal direct observations.

For Antarctic bedrock interpolation, mass conserving schemes use the local velocity field as an input data-stream. This can result in anisotropic interpolation performance between the along streamline and across flow directions (e.g. Roberts et al., 2011). As SMUG only uses observed bedrock elevations, it does not suffer from streamline anisotropy, but may suffer from anisotropic effects due to the distribution of observations, such as the region shown in Fig. 7.

In addition to producing interpolations, SMUG also calculates the associated uncertainties using a combination of contributions from the ensemble (using different points for both the derivative calculation and the origin of the Taylor series expansion), and the uncertainty in the observations. In the context of producing and utilising an Antarctic bedrock estimation, these uncertainties have several direct applications, notably: (1) quantifying where bed topography is most uncertain, given the current distribution of the observations; (2) for use as boundary conditions in ice sheet models to assess where uncertainties have the greatest impact on ice dynamics, and the associated Antarctic contribution to local and global sea-level change; (3) based on the outputs of both of the previous applications, designing future observational campaigns to meaningfully reduce uncertainties around Antarctica's sea-level contributions; and (4) for comparison with other interpolation algorithms to assess their corresponding skilfulness and robustness.

Robust interpolation uncertainty estimates (such as those produced by SMUG), are still subject to errors, biases and limitations associated with the underlying algorithm, its assumptions, and the distribution, errors and uncertainties in the observations. One potentially useful approach to reduce and/or quantify these errors and biases is to produce interpolations using a multi-model ensemble built on different algorithms, with the final interpolation being based on robust statistical measures of the central tendency and spread of the multi-model ensemble (see, for example in an process optimisation context, Liu, 2018). With the use of robust statistical measures (such as the median or M-estimator), such multi-model ensembles are largely unaffected by outliers. In addition, the individual model estimated uncertainties can be used to inverse-weight the final interpolation to de-emphasise models with large uncertainties.

The main user-configurable parameter for SMUG is the order of the Taylor series expansion. As for polynomial interpolation, in general using the lowest order interpolation that is consistent with the data will produce the best results, i.e. typically first order SMUG interpolation is appropriate, although in some circumstances second order might perform better. At high observational density (and associated small interpolation distances), the differences between first and second order interpolations should be small. In fact, even at the (locally) relatively large observational data spacing over the Aurora Subglacial Basin, the differences in the interpolated bed topography using both first and second order interpolation are small (compare Figures 1 and 5). Due to the additional terms in the Taylor series expansion (Equation 2), the generally larger weighting coefficients that arise in higher-order meshless derivative calculations

338 (e.g. Abramowitz and Stegun, 1968; Roberts, 2008), and the monotonically increasing behaviour of the ball-arithmetic  
339 uncertainty (Equation 3), the uncertainty estimates for second order interpolations will be larger than for first order.

340 **5. Conclusions**

341 We present a new method for interpolating sparse and unevenly sampled spatial data with robust uncertainty es-  
342 timates, namely the Stochastic Meshless Uncertainty Gridding (SMUG) algorithm. To demonstrate its performance,  
343 we apply SMUG to reconstruct the bed topography of the Aurora Subglacial Basin in East Antarctica. As with all  
344 interpolation approaches, SMUG is subject to artefacts arising from the quality of input data and can introduce im-  
345 pulse noise in the resulting interpolated data field. While such issues can be partly mitigated through quality control  
346 of the input data and varying the ensemble size, challenges will persist where observational coverage is limited. A key  
347 strength of SMUG lies in its ability to produce robust, ensemble-based uncertainty estimates. Future work could ex-  
348 plore extensions such as meta-ensembles that combine multiple algorithms to further improve accuracy and uncertainty  
349 characterisation.

350 **6. Acknowledgements**

351 This research was supported by the Australian Research Council (ARC) Special Research Initiative (SRI) Securing  
352 Antarctica's Environmental Future (SR200100005) and an ARC Discovery Early Career Award (DE210101433).

353 **Code availability section**

354 FORTRAN source code for SMUG is available for download under the GPLv3 licence at <https://github.com/jlr581/SMUG>.  
 355 The meshless library code SMUG uses is included within this repository, but is also available at  
 356 [https://github.com/jlr581/finite\\_difference](https://github.com/jlr581/finite_difference).

357 **A. Supplementary figures**358 **References**

- 359 Abramowitz, M., Stegun, I. (Eds.), 1968. Handbook of Mathematical Functions. United States Department of Commerce, Washington.
- 360 Frémand, A.C., Fretwell, P., Bodart, J.A., Pritchard, H.D., Aitken, A., Bamber, J.L., Bell, R., Bianchi, C., Bingham, R.G., Blankenship, D.D.,  
 361 Casassa, G., Catania, G., Christianson, K., Conway, H., Corr, H.F.J., Cui, X., Damaske, D., Damm, V., Drews, R., Eagles, G., Eisen, O.,  
 362 Eisermann, H., Ferraccioli, F., Field, E., Forsberg, R., Franke, S., Fujita, S., Gim, Y., Goel, V., Gogineni, S.P., Greenbaum, J., Hills, B.,  
 363 Hindmarsh, R.C.A., Hoffman, A.O., Holmlund, P., Holschuh, N., Holt, J.W., Horlings, A.N., Humbert, A., Jacobel, R.W., Jansen, D., Jenkins,  
 364 A., Jokat, W., Jordan, T., King, E., Kohler, J., Krabill, W., Kusk Gillespie, M., Langley, K., Lee, J., Leitchenkov, G., Leuschen, C., Luyendyk, B.,  
 365 MacGregor, J., MacKie, E., Matsuoka, K., Morlighem, M., Mouginot, J., Nitsche, F.O., Nogi, Y., Nost, O.A., Paden, J., Pattyn, F., Popov, S.V.,  
 366 Rignot, E., Rippin, D.M., Rivera, A., Roberts, J., Ross, N., Ruppel, A., Schroeder, D.M., Siegert, M.J., Smith, A.M., Steinhage, D., Studinger,  
 367 M., Sun, B., Tabacco, I., Tinto, K., Urbini, S., Vaughan, D., Welch, B.C., Wilson, D.S., Young, D.A., Zirizzotti, A., 2023. Antarctic Bedmap  
 368 data: Findable, Accessible, Interoperable, and Reusable (FAIR) sharing of 60 years of ice bed, surface, and thickness data. Earth System Science  
 369 Data 15, 2695–2710. doi:10.5194/essd-15-2695-2023.
- 370 Fretwell, P., Pritchard, H.D., Vaughan, D.G., Bamber, J.L., Barrand, N.E., Bell, R., Bianchi, C., Bingham, R.G., Blankenship, D.D., Casassa,  
 371 G., Catania, G., Callens, D., Conway, H., Cook, A.J., Corr, H.F.J., Damaske, D., Damm, V., Ferraccioli, F., Forsberg, R., Fujita, S., Gim, Y.,  
 372 Gogineni, P., Griggs, J.A., Hindmarsh, R.C.A., Holmlund, P., Holt, J.W., Jacobel, R.W., Jenkins, A., Jokat, W., Jordan, T., King, E.C., Kohler,  
 373 J., Krabill, W., Riger-Kusk, M., Langley, K.A., Leitchenkov, G., Leuschen, C., Luyendyk, B.P., Matsuoka, K., Mouginot, J., Nitsche, F.O., Nogi,  
 374 Y., Nost, O.A., Popov, S.V., Rignot, E., Rippin, D.M., Rivera, A., Roberts, J., Ross, N., Siegert, M.J., Smith, A.M., Steinhage, D., Studinger,  
 375 M., Sun, B., Tinto, B.K., Welch, B.C., Wilson, D., Young, D.A., Xiangbin, C., Zirizzotti, A., 2013. Bedmap2: improved ice bed, surface and  
 376 thickness datasets for Antarctica. The Cryosphere 7, 375–393. doi:10.5194/tc-7-375-2013.
- 377 Graham, F.S., Roberts, J.L., Galton-Fenzi, B.K., Young, D., Blankenship, D., Siegert, M.J., 2017. A high-resolution synthetic bed elevation grid of  
 378 the Antarctic continent. Earth System Science Data 9, 267–279. doi:10.5194/essd-9-267-2017.
- 379 Johansson, F., 2020. Ball arithmetic as a tool in computer algebra, in: Gerhard, J., Kotsireas, I. (Eds.), Maple in Mathematics Education and  
 380 Research, Springer International Publishing, Cham. pp. 334–336.
- 381 Kenichi Matsuoka, Geir Moholdt, J.F.A.J.A.B.X.C.F.R.F.V.G.T.A.J.F.S.M.R.M.H.D.P.C.S.K.T.F.B.M.G.P.C.R.D.P.D.J.E.O.E.H.E.A.S.G.C.A.G.N.H.S.S.R.J.  
 382 . Towards an improved understanding of the antarctic coastal zone and its contribution to future global sea level .
- 383 Liu, K.N., 2018. A multi-model ensemble approach to process optimization considering model uncertainty. Journal of Industrial and Production  
 384 Engineering 35, 550–557. doi:10.1080/21681015.2018.1534756.
- 385 Lythe, M.B., Vaughan, D.G., 2001. BEDMAP: A new ice thickness and subglacial topographic model of Antarctica. Journal of Geophysical  
 386 Research: Solid Earth 106, 11335–11351. URL: <https://agupubs.onlinelibrary.wiley.com/doi/abs/10.1029/2000JB900449>,  
 387 doi:<https://doi.org/10.1029/2000JB900449>.
- 388 M. Morlighem, C. N. Williams, E.R.L.A.J.E.A.J.L.B.G.C.N.C.J.A.D.B.D.I.F.K.H.I.H.A.H.M.J.T.M.J.K.K.R.M.L.M.J.M.B.P.Y.N.C.O.S.P.S.R.H.S.M.J.S.P.S.

## Stochastic Meshless Uncertainty Gridding

- 389 2017. Bedmachine v3: Complete bed topography and ocean bathymetry mapping of greenland from multibeam echo sounding combined with  
390 mass conservation. *Geophysical Research Letters* 44, 10051–11061. doi:10.1002/2017GL074954.
- 391 MacKie, E.J., Schroeder, D.M., 2020. Geostatistically simulating subglacial topography with synthetic training data, in: IGARSS 2020 - 2020 IEEE  
392 International Geoscience and Remote Sensing Symposium, pp. 2991–2994. doi:10.1109/IGARSS39084.2020.9324563.
- 393 MacKie, E.J., Schroeder, D.M., Zuo, C., Yin, Z., Caers, J., 2021. Stochastic modeling of subglacial topography exposes uncertainty in water routing  
394 at Jakobshavn Glacier. *Journal of Glaciology* 67, 75–83. doi:10.1017/jog.2020.84.
- 395 McCormack, F.S., Stål, T., Shao, N., MacKie, E., Hinojosa, A.F., Lösing, M., Roberts, J.L., Ehrenfeucht, S., Dow, C.F., Submitted. Synthetic bed  
396 topographies for Antarctica and their utility in ice sheet modelling. *Proceedings of the Royal Society A* .
- 397 Mitas, L., Mitasova, H., 1999. Spatial Interpolation. *GeoInformation International*, Wiley. chapter 34. pp. 481–492.
- 398 Morlighem, M., Rignot, E., Binder, T., Blankenship, D., Drews, R., Eagles, G., Eisen, O., Ferraccioli, F., Forsberg, R., Fretwell, P., Goel, V.,  
399 Greenbaum, J.S., Gudmundsson, H., Guo, J., Helm, V., Hofstede, C., Howat, I., Humbert, A., Jokat, W., Karlsson, N.B., Lee, W.L., Matsuoka,  
400 K., Millan, R., Mouginot, J., Paden, J., Pattyn, F., Roberts, J., Rosier, S., Ruppel, A., Seroussi, H., Smith, E.C., Steinhage, D., Sun, B., van den  
401 Broeke, M.R., van Ommen, T.D., van Wessem, M., Young, D.A., 2020. Deep glacial troughs and stabilizing ridges unveiled beneath the margins  
402 of the Antarctic ice sheet. *Nature Geoscience* 13, 132–137. doi:10.1038/s41561-019-0510-8.
- 403 Morlighem, M., Rignot, E., Seroussi, H., Larour, E., Ben Dhia, H., Aubry, D., 2011. A mass conservation approach for mapping glacier ice  
404 thickness. *Geophysical Research Letters* 38. URL: <https://agupubs.onlinelibrary.wiley.com/doi/abs/10.1029/2011GL048659>,  
405 doi:<https://doi.org/10.1029/2011GL048659>.
- 406 Pritchard, H., Fretwell, P., Fremand, A., Bodart, J., Kirkham, J., Aitken, A., Bamber, J., Bell, R., Bianchi, C., Bingham, R., Blankenship, D.,  
407 Casassa, G., Catania, G., Christianson, K., Conway, H., Corr, H., Cui, X., Damaske, D., Damn, V., Dorschel, B., Drews, R., Eagles, G., Eisen,  
408 O., Eisermann, H., Ferraccioli, F., Field, E., Forsberg, R., Franke, S., Fujita, S., Gim, Y., Goel, V., Gogineni, S.P., Greenbaum, J., Hills, B.,  
409 Hindmarsh, R., Hoffman, A., Holmlund, P., Holschuh, N., Holt, J., Horlings, A., Humbert, A., Jacobel, R., Jansen, D., Jenkins, A., Jokat, W.,  
410 Jordan, T., King, E., Kohler, J., Krabill, W., Langley, K., Lee, J., Leitchenkov, G., Leuschen, C., Luyendyk, B., MacGregor, J., MacKie, E.,  
411 Matsuoka, K., Moholdt, G., Morlighem, M., Mouginot, J., Nitsche, F., Nogi, Y., Nost, O., Paden, J., Pattyn, F., Popov, S., Kusk-Gillespie, M.,  
412 Rignot, E., Rippin, D., Rivera, A., Roberts, J., Ross, N., Ruppel, A., Schroeder, D., Siegert, M., Smith, A., Steinhage, D., Studinger, M., Sun,  
413 B., Tabacco, I., Tinto, K., Urbini, S., Vaughan, D., Welch, B., Wilson, D., Young, D., Zirizzotti, A., 2024. BEDMAP3 - Ice thickness, bed and  
414 surface elevation for Antarctica - gridding products. URL: <https://data.bas.ac.uk/full-record.php?id=GB/NERC/BAS/PDC/01615>,  
415 doi:10.5285/2D0E4791-8E20-46A3-80E4-F5F6716025D2.
- 416 Pritchard, H.D., Fretwell, P.T., Fremand, A.C., Bodart, J.A., Kirkham, J.D., Aitken, A., Bamber, J., Bell, R., Bianchi, C., Bingham, R.G., Blanken-  
417 ship, D.D., Casassa, G., Christianson, K., Conway, H., Corr, H.F.J., Cui, X., Damaske, D., Damm, V., Dorschel, B., Drews, R., Eagles, G.,  
418 Eisen, O., Eisermann, H., Ferraccioli, F., Field, E., Forsberg, R., Franke, S., Goel, V., Gogineni, S.P., Greenbaum, J., Hills, B., Hindmarsh,  
419 R.C.A., Hoffman, A.O., Holschuh, N., Holt, J.W., Humbert, A., Jacobel, R.W., Jansen, D., Jenkins, A., Jokat, W., Jong, L., Jordan, T.A., King,  
420 E.C., Kohler, J., Krabill, W., Maton, J., Gillespie, M.K., Langley, K., Lee, J., Leitchenkov, G., Leuschen, C., Luyendyk, B., MacGregor, J.A.,  
421 MacKie, E., Moholdt, G., Matsuoka, K., Morlighem, M., Mouginot, J., Nitsche, F.O., Nost, O.A., Paden, J., Pattyn, F., Popov, S., Rignot,  
422 E., Rippin, D.M., Rivera, A., Roberts, J.L., Ross, N., Ruppel, A., Schroeder, D.M., Siegert, M.J., Smith, A.M., Steinhage, D., Studinger, M.,  
423 Sun, B., Tabacco, I., Tinto, K.J., Urbini, S., Vaughan, D.G., Wilson, D.S., Young, D.A., Zirizzotti, A., 2025. Bedmap3 updated ice bed, sur-  
424 face and thickness gridded datasets for Antarctica. *Scientific Data* 12, 414. URL: <https://doi.org/10.1038/s41597-025-04672-y>,  
425 doi:10.1038/s41597-025-04672-y.
- 426 Rignot, E., Mouginot, J., Scheuchl, B., 2011. Ice Flow of the Antarctic Ice Sheet. *Science* 333, 1427–1430. doi:10.1126/science.1208336.

## Stochastic Meshless Uncertainty Gridding

- 427 Rignot, E., Mouginot, J., Scheuchl, B., 2017. MEaSUREs InSAR-based Antarctica ice velocity map 450m V2.0. doi:10.5067/MEASURES/  
428 CRYOSPHERE/nsidc-0484.001.
- 429 Roberts, J., 2008. A method for calculating meshless finite difference weights. International Journal for Numerical Methods in Engineering 74,  
430 321–336. doi:/10.1002/nme.2169.
- 431 Roberts, J.L., 2024. Meshless weighting coefficients for arbitrary nodes: The efficient computation to machine precision using hyper-dual numbers.  
432 Advances in Engineering Software 197, 103753. doi:10.1016/j.advengsoft.2024.103753.
- 433 Roberts, J.L., Warner, R.C., Young, D., Wright, A., van Ommen, T.D., Blankenship, D.D., Siegert, M., Young, N.W., Tabacco, I.E., Forieri, A.,  
434 Passerini, A., Zirizzotti, A., Frezzotti, M., 2011. Refined broad-scale sub-glacial morphology of Aurora Subglacial Basin, East Antarctica derived  
435 by an ice-dynamics-based interpolation scheme. The Cryosphere 5, 551–560. doi:10.5194/tc-5-551-2011.
- 436 Smirnov, P.O., Shevlyakov, G.L., 2014. Fast highly efficient and robust one-step M-estimators of scale based on Qn. Computational Statistics &  
437 Data Analysis 78, 153–158. doi:10.1016/j.csda.2014.04.013.
- 438 Smith, B., Fricker, H.A., Gardner, A.S., Medley, B., Nilsson, J., Paolo, F.S., Holschuh, N., Adusumilli, S., Brunt, K., Csatho, B., Harbeck, K.,  
439 Markus, T., Neumann, T., Siegfried, M.R., Zwally, H.J., 2020. Pervasive ice sheet mass loss reflects competing ocean and atmosphere processes.  
440 Science 368, 1239–1242. doi:10.1126/science.aaz5845.
- 441 Webster, R., Oliver, M., 2007. Geostatistics for Environmental Scientists. Wiley. doi:10.1002/9780470517277.
- 442 Wilcox, R.R., 2010. Fundamentals of Modern Statistical Methods. Springer-Verlag, New York. doi:10.1007/978-1-4419-5525-8.

443 **List of Figures**

444 1	Antarctic bed topography reconstruction at 500m horizontal resolution, and differences from published 445 interpolations. A) SMUG interpolation, with 500m elevation contours shown in grey. B) Interpolation 446 uncertainty and observational data locations (blue points). C) SMUG minus Bedmap3 Pritchard et al. 447 (2025). D) SMUG minus Bedmachine V2 Morlighem et al. (2020) . . . . .	17
448 2	Denman Glacier local region. A) SMUG interpolation, B) Bedmap3 interpolation, C) BedMachine 449 interpolation, D) Bedmap3 observational data, E) MEaSUREs version 2 surface speed (Rignot et al., 450 2011, 2017), F) longitudinal strain rate from MEaSUREs version 2 surface velocity, G) transect Ta– 451 Tb showing SMUG (gray shading shows uncertainty), Bedmap3, BedMachine bed profiles, and the 452 observations. . . . .	18
453 3	Impact of excluding local data on the interpolation compared to no data exclusion at 1 km resolution. 454 Shown are the mean difference (circle), $\pm$ one standard deviation (error bars) and lower quartile, 455 median and upper quartile (boxes). . . . .	19
456 4	Antarctic bed topography (first and third rows) at 1 km horizontal resolution, with observational data 457 excluded, and corresponding difference from interpolation without data exclusion (second and forth 458 rows). Data exclusion radius 5 km (A and D), 10 km (B and E), 20 km (C and F), 30 km, (G and J), 459 40 km (H and K) and 50 km (I and L). . . . .	20
460 5	2nd order Taylor interpolation of ASB at 1 km reconstruction, raw interpolation. A) Bedrock topog- 461 raphy, and B) interpolation uncertainty (grey-scale) and observational data locations (blue points). . . .	21
462 6	The bed topography dataset after a median filter has been applied to remove impulse noise. The blue 463 star indicates the location of the deepest topography and the red star the highest point in the bedrock. . .	22
464 7	Example of anisotropic effects due to distribution of observations, noting the striping present and dis- 465 continuity where there are fewer observations. . . . .	23

### Stochastic Meshless Uncertainty Gridding

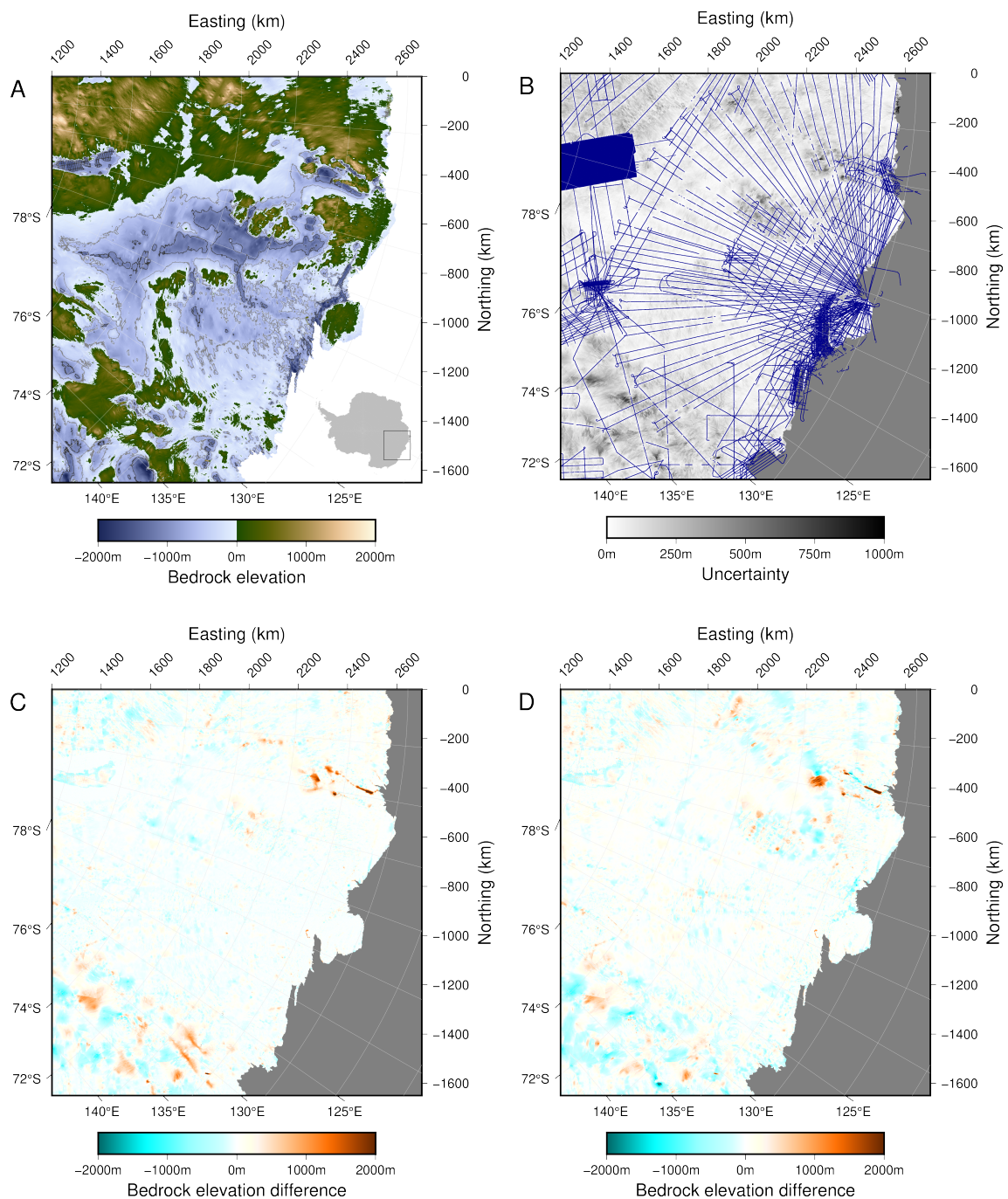


**Figure 1:** Antarctic bed topography reconstruction at 500m horizontal resolution, and differences from published interpolations. A) SMUG interpolation, with 500m elevation contours shown in grey. B) Interpolation uncertainty and observational data locations (blue points). C) SMUG minus Bedmap3 Pritchard et al. (2025). D) SMUG minus BedMachine V2 Morlighem et al. (2020)

## Stochastic Meshless Uncertainty Gridding

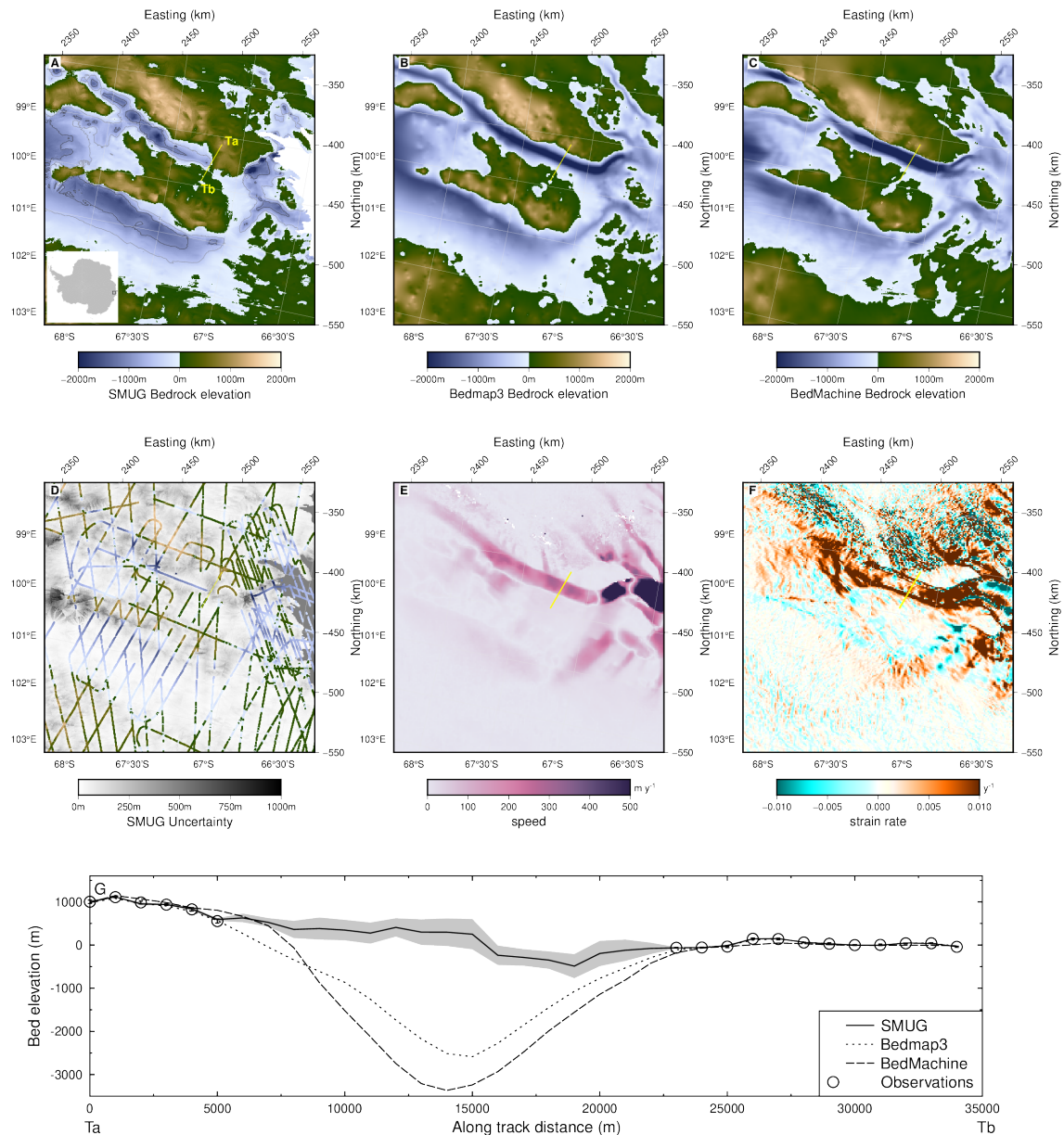


**Figure 2:** Denman Glacier local region. A) SMUG interpolation, B) Bedmap3 interpolation, C) BedMachine interpolation, D) Bedmap3 observational data, E) MEaSUREs version 2 surface speed (Rignot et al., 2011, 2017), F) longitudinal strain rate from MEaSUREs version 2 surface velocity, G) transect Ta-Tb showing SMUG (gray shading shows uncertainty), Bedmap3, BedMachine bed profiles, and the observations.

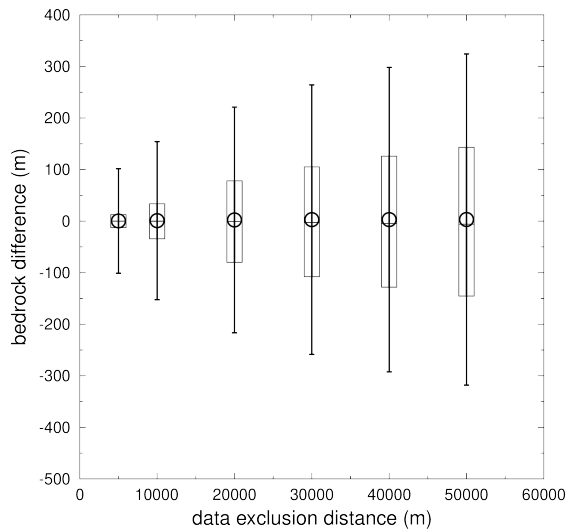


**Figure 3:** Impact of excluding local data on the interpolation compared to no data exclusion at 1 km resolution. Shown are the mean difference (circle),  $\pm$  one standard deviation (error bars) and lower quartile, median and upper quartile (boxes).

## Stochastic Meshless Uncertainty Gridding

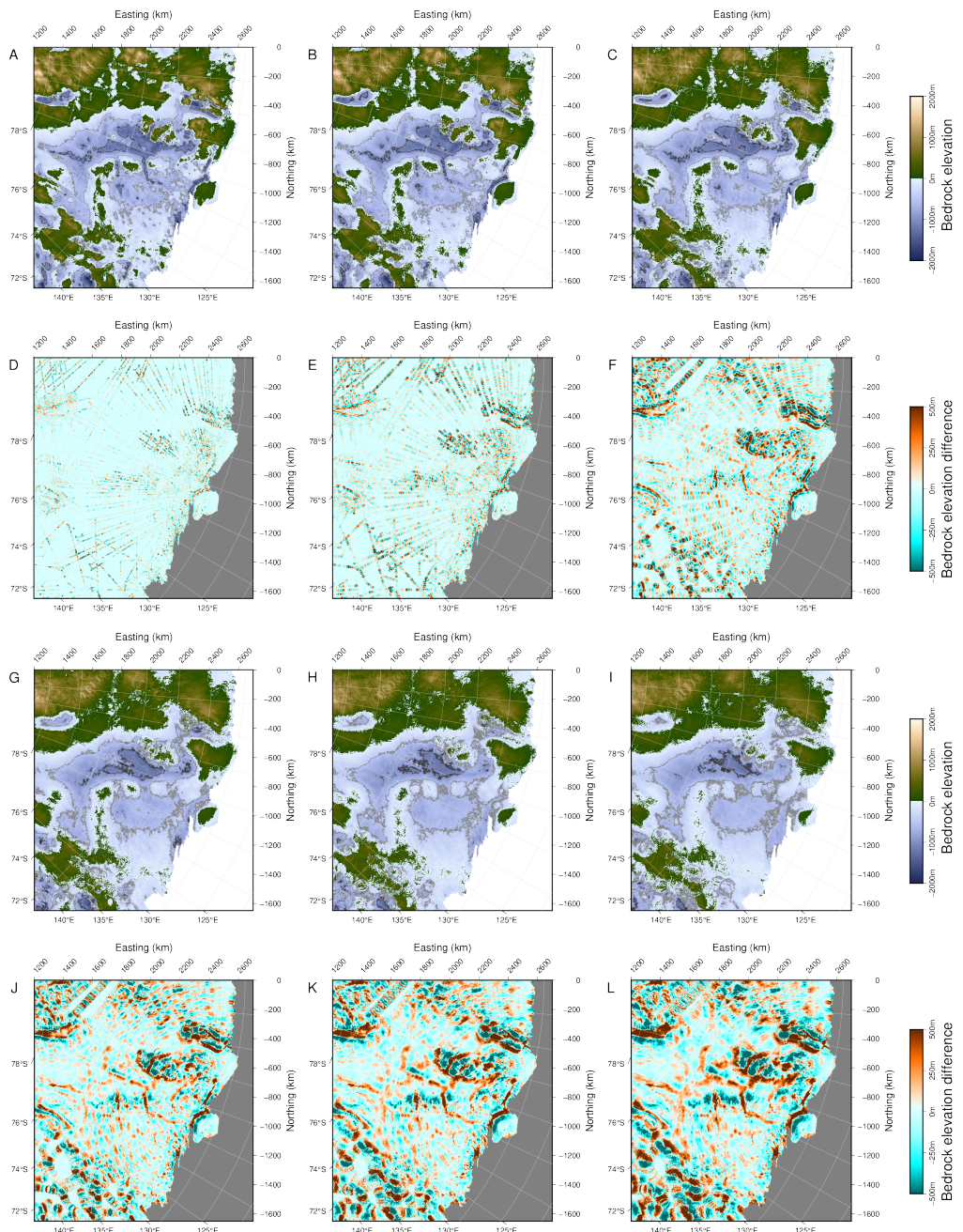


**Figure 4:** Antarctic bed topography (first and third rows) at 1 km horizontal resolution, with observational data excluded, and corresponding difference from interpolation without data exclusion (second and forth rows). Data exclusion radius 5 km (A and D), 10 km (B and E), 20 km (C and F), 30 km, (G and J), 40 km (H and K) and 50 km (I and L).

### Stochastic Meshless Uncertainty Gridding

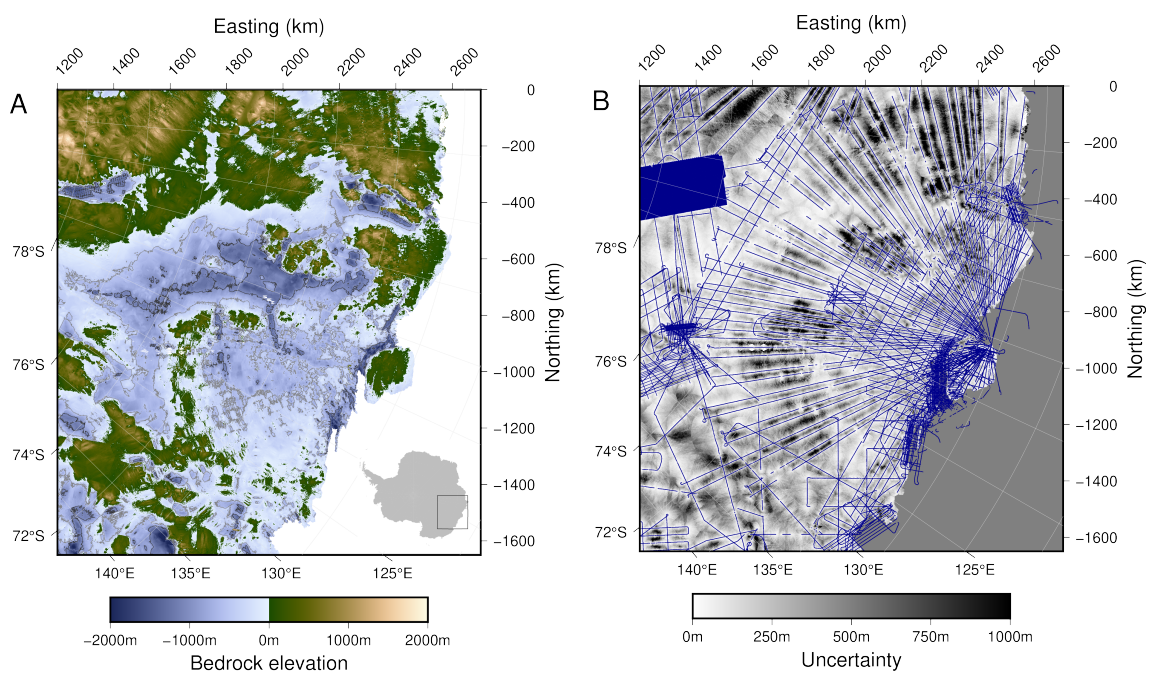


**Figure 5:** 2nd order Taylor interpolation of ASB at 1 km reconstruction, raw interpolation. A) Bedrock topography, and B) interpolation uncertainty (grey-scale) and observational data locations (blue points).

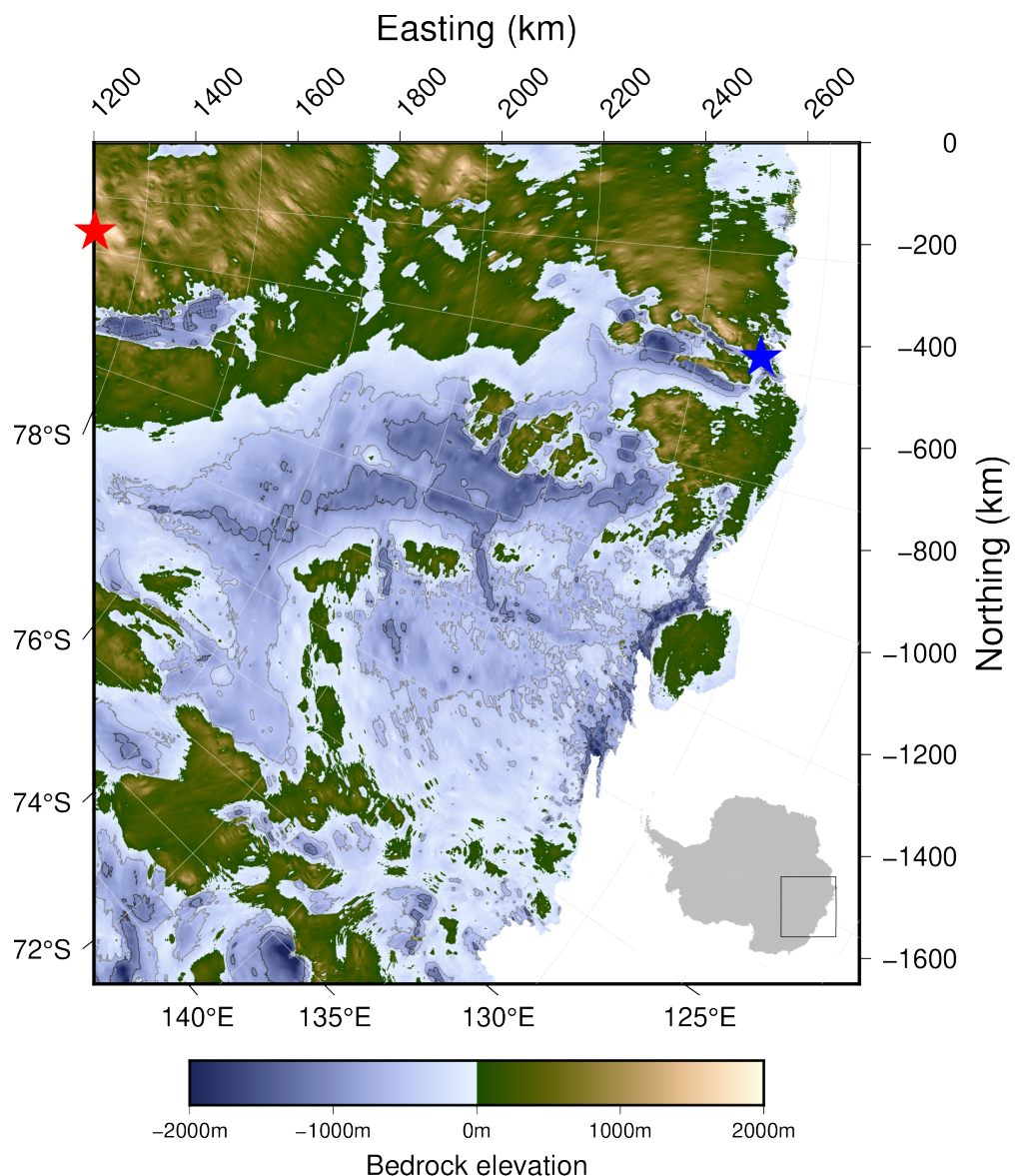


**Figure 6:** The bed topography dataset after a median filter has been applied to remove impulse noise. The blue star indicates the location of the deepest topography and the red star the highest point in the bedrock.

### Stochastic Meshless Uncertainty Gridding

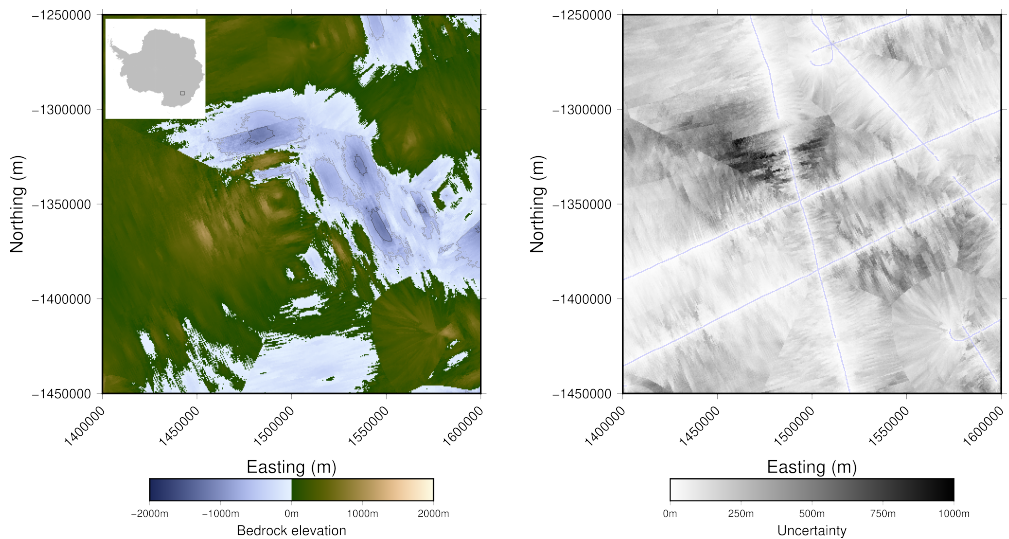


**Figure 7:** Example of anisotropic effects due to distribution of observations, noting the striping present and discontinuity where there are fewer observations.